Article ID: 1000-7032(2023)05-0819-18

Efficiently Narrow-band Perovskite-type Phosphor $K_2BaPO_4F:Eu^{2+}$ Based on Dual-sites-triggered Energy Transfer Behavior

ZHANG Rong[1,2], SUN Jianfeng[1,2*]

(1. *Key Laboratory of Special Functional Materials for Ecological Environment and Information (Hebei University of Technology), Ministry of Education, Tianjin* 300130, *China*;
2. *School of Materials Science and Engineering, Hebei University of Technology, Tianjin* 300130, *China*)
* *Corresponding Author, E-mail: sunjianfeng*10@*hebut. edu. cn*

Abstract: Along with the development of versatile trichromatic phosphors, exploring novel narrow-band blue-emitting phosphors has been an ongoing focus in liquid crystal display backlighting to satisfy the high-quality display demands. Herein, an intriguing narrow-band blue-emitting phosphor $K_2BaPO_4F:Eu^{2+}$ belonging to the perovskite-type structural prototype is synthesized *via* the solid-state reaction. Structural analysis indicates that the $[FK_4Ba_2]$ octahedra is interlinked with each other by sharing Ba and K atoms to build a three-dimensional network together with $[PO_4]$ tetrahedra in the cavities. Rietveld refinement analysis shows that the Eu^{2+} ions reside in both Ba^{2+} and K^+ sites to form the $[Eu(1)O_8F_2]$ and $[Eu(2)O_6F_2]$ polyhedra, which totally induce an intense blue emission peaking at 432 nm with a narrow full width at half-maximum of 43 nm, theoretically verified by the dipole-dipole interaction in the Eu(1)→Eu(2) energy transfer process. The electronic structure of K_2BaPO_4F matrix is studied by the first-principle calculation on the basis of the density functional theory, demonstrating that it has a large indirect band of 5. 035 eV. The $K_2BaPO_4F:Eu^{2+}$ phosphor exhibits a suitable thermal stability ($I_{493\ K}/I_{293\ K}$=64%) and possesses the satisfactory internal/external quantum efficiency of 72. 8%/46. 4%, which although is inferior to that of the representative $BaMgAl_{10}O_{17}:Eu^{2+}$, $K_{1.6}Al_{11}O_{17+\delta}:Eu^{2+}$ and $Na_3Sc_2(PO_4)_3:Eu^{2+}$ phosphors, yet surpasses some other recently reported blue-emitting phosphors. Consequently, the present work not only demonstrates the potential of $K_2BaPO_4F:Eu^{2+}$ phosphor as a new narrow-band blue-emitting phosphor candidate, but provides the possibility for exploring the novel phosphors inspired by the mineral-type structural prototypes.

Key words: perovskite-type structure; $K_2BaPO_4F:Eu^{2+}$; energy transfer; photoluminescence
CLC number: O482. 31 **Document code**: A **DOI**: 10. 37188/CJL. 20220412

基于双发光位点能量传递构建高效窄带钙钛矿构型 $K_2BaPO_4F:Eu^{2+}$荧光粉

张 荣[1,2], 孙剑锋[1,2*]

(1. 生态环境和信息特种功能材料教育部重点实验室(河北工业大学), 天津 300130;
2. 河北工业大学 材料科学与工程学院, 天津 300130)

摘要: 随着近紫外芯片激发三基色荧光粉技术的发展,开发用于液晶显示背光源以满足高品质显示需求的新型窄带蓝色荧光粉已经成为材料研究者日益关注的焦点。本文采用高温固相法合成了具有钙钛矿结构原型

收稿日期: 2022-12-12; **修订日期**: 2023-01-03
基金项目: 通辽市引导科技创新激励基金
Supported by Incentive Fund Project for Guiding Scientific and Technological Innovation of Tongliao City

的 $K_2BaPO_4F:Eu^{2+}$窄带蓝色荧光粉。K_2BaPO_4F基质由[FK_4Ba_2]八面体以共享 Ba、K 原子的方式相连形成三维网状阴离子框架,进而与孔道中的[PO_4]四面体连接形成 K_2BaPO_4F钙钛矿结构框架。Rietveld精修分析表明,Eu^{2+}同时占据 Ba^{2+}和 K^+位点形成[Eu(1)O_8F_2]和[Eu(2)O_6F_2]配位多面体,两种多面体发光中心存在由偶极-偶极效应引起的 Eu(1)→Eu(2)能量传递过程,使荧光粉具有发射峰值波长为 432 nm、半峰宽为 43 nm 的高亮度窄带蓝光发射。基于密度泛函理论的第一性原理计算表明,K_2BaPO_4F基质为间接带隙化合物,理论带隙值为 5.035 eV。$K_2BaPO_4F:Eu^{2+}$荧光粉展现了合适的荧光热稳定性($I_{493\ K}/I_{293\ K}$=64%)和较高的内、外量子效率(分别为 72.8% 和 46.4%),其性能指标虽然劣于 $BaMgAl_{10}O_{17}:Eu^{2+}$、$K_{1.6}Al_{11}O_{17+\delta}:Eu^{2+}$、$Na_3Sc_2(PO_4)_3:Eu^{2+}$等典型蓝粉,但优于其他一些已报道的蓝色荧光粉。上述研究工作不仅展现了 $K_2BaPO_4F:Eu^{2+}$作为一种新型窄带蓝色荧光粉的应用潜力,而且也为基于矿物结构原型策略探索新型荧光粉提供了可能性。

关 键 词:钙钛矿型结构;$K_2BaPO_4F:Eu^{2+}$;能量传递;光致发光

1 Introduction

Phosphor-converted light-emitting diodes (pc-LEDs) have been recognized as a key enabler for the emerging backlighting technology used in modern display devices such as liquid crystal displays (LCDs) owing to their superiorities of rapid response, tunable color, and high visual quality[1]. For the pc-LED backlighting technology used in LCDs, color gamut is a particularly significant performance index that can determine the color reproducibility of LCD devices, which is determined by the color space constructed by the red, green, and blue(RGB) emissions of LEDs passing through the corresponding RGB color filters[2]. The RGB phosphors with a narrow emission bandwidth(full width at half-maximum (FWHM) ≤ 60 nm) can ensure that most of their emissions pass through the RGB color filters instead of being excluded, which contributes to the improvement of color gamut[3]. Therefore, in order to obtain the wide color gamut, exploring narrow-band RGB phosphors to reduce the emissions excluded by RGB color filters is the focus of developing LED backlighting technology for LCDs. Until recently, a series of UCr_4C_4-type nitrides and silicates based on the design strategy of natural mineral structures, *e. g.*, Sr-[Mg_3SiN_4]: Eu^{2+} (λ_{max}=615 nm, FWHM=43 nm)[4], (Sr, Ca) [$LiAl_3N_4$]: Eu^{2+} (λ_{max}=654 nm, FWHM=52 nm for Sr[$LiAl_3N_4$]: Eu^{2+}; λ_{max}=668 nm, FWHM=60 nm for Ca[$LiAl_3N_4$]: Eu^{2+})[5-6], Rb(Li, Na)[Li_3SiO_4]$_2$: Eu^{2+}(λ_{max}=530 nm, FWHM=42 nm for RbLi[Li_3SiO_4]$_2$: Eu^{2+}; λ_{max}=523 nm, FWHM=41 nm for RbNa[Li_3SiO_4]$_2$: Eu^{2+})[2,7], $NaLi_3SiO_4:Eu^{2+}$ (λ_{max}=469 nm, FWHM=32 nm)[8], $RbNa_3[Li_3SiO_4]_4:Eu^{2+}$ (λ_{max}=471 nm, FWHM=22 nm)[9], have been developed as narrow-band RGB phosphors. Their common structural features, *viz.*, highly structural rigidity induced by small polyhedral units and symmetrical coordination environment of activators as well as uniform coordinating elements, not only hinder the occurrence of the structural relaxation of Eu^{2+} in its excited state to resist the thermal quenching behavior, but endow these phosphors with the narrow emission bandwidth. Learning from hieratite and cryolite-type prototype structures has also contributed to discovering narrow red-emitting Mn^{4+}-activated fluoride phosphors, for instance, $K_2(Ti,Si)F_6:Mn^{4+}$(λ_{max}=630 nm, FWHM=30 nm)[10-11], $K_2NaAlF_6:Mn^{4+}$ (λ_{max}=631 nm, FWHM=30 nm)[12], $Na_3GaF_6:Mn^{4+}$ (λ_{max}=626 nm, FWHM=28 nm)[13], all of which are constructed by three-dimensional network with regular arrangement of sharing-vertex [MF_6] octahedra, thereby offering the octahedral local coordination environment of Mn^{4+} in favor of its efficiently red emission ($K_2(Ti,Si)F_6:Mn^{4+}$, internal quantum efficiency(IQE) η_{IQE}=92%-98%; $K_2NaAlF_6:Mn^{4+}$, η_{IQE}=89%; $Na_3GaF_6:Mn^{4+}$, η_{IQE}=69%)[10,12-14]. Some of the above mentioned fluoride phosphors further exhibit the ideal thermal stability owing to the abnormal thermal quenching behavior deriving from the unit cell expansion of fluoride hosts and the vibration modes enhancement from Mn^{4+} under high temperature, which eventually benefit to utilize them as the narrow red component[10]. Distinguished from aforementioned UCr_4C_4-type and hieratite/cryolite-

type narrow-band phosphors, Ce^{3+}-doped garnet-type phosphors typified by the yttroalumite ($Y_3Al_5O_{12}$) structural prototype tend to emit wide-band fluorescence with the varied colors depending on a wide range of inorganic elements in its adaptable structure framework, such as $(Y,Lu)_3Al_5O_{12}:Ce^{3+}$ (λ_{max}=505–532 nm)[15-16], $MgY_2Al_4SiO_{12}:Ce^{3+}$ (λ_{max}=566 nm)[17], $Lu_3(Al,Mg)_2(Al,Si)_3O_{12}:Ce^{3+}$ (λ_{max}=542–571 nm)[18], and $Lu_2CaMg_2(Si,Ge)_3O_{12}:Ce^{3+}$ (λ_{max}=605 nm)[19]. Definitely, this design principle based on different natural mineral-inspired structures is timesaving and effective, which is not only conducive to discovering new chemical phases for seeking novel luminescent materials, but can be adopted to regulate luminescence properties associated with structures.

Based on such a structural engineering strategy, the fascinating perovskite-type compounds have aroused scientists' interest due to the compositional diversity with a variety of elements in the general ABX_3 stoichiometry[20]. The burgeoning lead-based organohalide perovskites(*e. g.*, $CH_3NH_3PbX_3$, X=Cl, Br, I) or all-inorganic halide perovskites(*e. g.*, $CsPbX_3$, X=Cl, Br, I) have recently emerged as the promising photoelectric materials applied in solar cells or quantum-dot LEDs[21-22]. Meantime continuous research is ongoing to develop novel rare-earth/transition-metal ions-activated perovskite-type phosphors with favorable luminescence performance packaged in display and solid-state lighting devices. For instance, both double perovskite $Cs_2(Li,Na)BiCl_6:Mn^{2+}$ and quadruple perovskite $Cs_4CdBi_2Cl_{12}:Mn^{2+}$ phosphors exhibit the broad orange-red emission peaking at 590–612 nm *via* the spin-forbidden $^4T_1(G)$-$^6A_1(S)$ transition of Mn^{2+} attributing to the energy transfer from Bi^{3+} to Mn^{2+}, demonstrating their potential applications in the field of solid-state lighting[23-25]. In the sight of structural evolution for the substitution $4[MgF_6]=3[MgF_6]+[CaF_6]$ in the $CsMgF_3$ structure, our group further developed a novel perovskite-type blue-emitting $Cs_4Mg_3CaF_{12}:Eu^{2+}$ phosphor (λ_{max}=474 nm), which possessed a satisfactory thermal stability ($I_{473\,K}/I_{298\,K}$=80%) and a higher η_{IQE} of 64%, being competently served as the blue component to fabricate the near-ultraviolet (near-UV)-pumped WLEDs[26]. Nonetheless, the above two phosphors both exhibit the wide emission band with relatively large FWHM, limiting their further applications in the field of LCD backlighting. Until recently, a series of perovskite-type phosphate fluorides M_2CaPO_4F (M=K, Rb), which belong to the *Pnma* space group, have also been discovered by combing mineral-type structural prototype with isovalent substitution[27]. Both of them are constructed by one-dimensional perovskite-type $[FM_2Ca]_\infty$ chains consisted of face-sharing $[FM_4Ca_2]$ octahedra, which connect with $[PO_4]$ tetrahedra to build the structural framework. The introduction of Eu^{2+} activator not only endows the phosphors ($K_2CaPO_4F:Eu^{2+}$ and $(Rb,K)_2CaPO_4F:Eu^{2+}$) with a wide range of multicolor spectral modulation owing to the site-selective occupation of Eu^{2+} among different cation sites manipulated by different Eu^{2+}-doping concentrations, synthesis temperatures or alkaline-metal substitution, but also enables the broad emission band of $Rb_2CaPO_4F:Eu^{2+}$ phosphor to fill the "cyan gap" towards full-visible-spectrum lighting[28-31]. Unlike the isostructural phosphate fluorides M_2CaPO_4F (M=K, Rb), another perovskite-type K_2BaPO_4F (KBPOF) compound adopts the three-dimensional structure with interlinked F-centered $[FK_4Ba_2]$ octahedra (B-site) connected by $[PO_4]$ tetrahedra (A-site), which is analogous to the cubic ABX_3 perovskite-type structure[32]. By introducing Eu^{2+} ion into KBPOF host lattice, we herein synthesize the perovskite-type blue-emitting phosphor $KBPOF:Eu^{2+}$ induced by the energy transfer process between two luminescence centers, which exhibits the narrow-band emission characteristic (FWHM=42 nm) and is comparable to some currently emerged UCr_4C_4-type narrow-band blue phosphors such as $NaLi_3SiO_4:Eu^{2+}$ (λ_{max}=469 nm, FWHM=32 nm)[8], $RbNa_3[Li_3SiO_4]_4:Eu^{2+}$ (λ_{max}=471 nm, FWHM=22 nm)[9], and $(Rb,Cs)Na_2K[Li_3SiO_4]_4:Eu^{2+}$ (λ_{max}=480–485 nm, FWHM=26 nm)[33]. Although our developed $KBPOF:Eu^{2+}$ phosphor does not exhibit the zero-thermal-quenching behavior as previously reported by Leng *et al.* [34] and is inferior to the representative blue phosphors such as $K_{1.6}Al_{11}O_{17+\delta}:Eu^{2+}$[35] and $Na_3Sc_2(PO_4)_3:$

Eu^{2+}[36], it still possesses the suitable thermal stability ($I_{493\,K}/I_{298\,K}$=64%) and remarkable η_{IQE} up to 72.8%, significantly surpassing some other recently reported blue phosphors, *e. g.*, $Ba_9Lu_2Si_6O_{24}:Eu^{2+}$ (I_{473K}/I_{298K}=18%, η_{IQE}=68%)[37], $KBaYSi_2O_7:Eu^{2+}$ ($I_{473\,K}/I_{298\,K}$=10%, η_{IQE}=35%)[38], and $Ba_2Y_5B_5O_{17}:Bi^{3+}$ ($I_{473\,K}/I_{298\,K}$<50%, η_{IQE}=46%)[39]. Our present study also aims to provide the further understanding of the intrinsic thermal quenching effect of KBPOF:Eu^{2+} by systematically analyzing the temperature-dependent luminescence behaviors of different Eu^{2+} luminescence centers, which is not only yet unexplored by Leng *et al.*, but is conducive to clarifying the existing issue on the thermal quenching behavior of the perovskite-type KBPOF:Eu^{2+} phosphor. In addition, other investigations such as the electronic band structure of KBPOF and microscopic coordination environments of two Eu^{2+} luminescence centers as well as the mechanisms on the energy transfer process and concentration quenching behavior are also systematically performed. The present study based on the mineral-inspired structures can provide the further understanding for developing unique narrow-band blue-emitting phosphors applicable in LEDs as the components of LCD backlighting devices.

2 Experiment

2.1 Materials and Synthesis

The KBPOF:$x Eu^{2+}$ (x=0–0.10) samples were prepared by a conventional solid-state reaction. Firstly, all starting materials of KF (analytical reagent (A. R.); Tianjin Sailboats Chemical Reagent Co. Ltd., Tianjin, China), K_2CO_3 (A. R.; Tianjin Bodi Chemical Co. Ltd., Tianjin, China), $BaCO_3$ (A. R.; Tianjin Sailboats Chemical Reagent Co. Ltd., Tianjin, China), $NH_4H_2PO_4$ (A. R.; Tianjin Bodi Chemical Co. Ltd., Tianjin, China) were weighted based on the stoichiometric ratio (KF:K_2CO_3:$BaCO_3$:$NH_4H_2PO_4$=2:1:2:2). Secondly, all raw materials were uniformly mixed in agate mortars, and the mixtures were further transferred into the corundum crucibles. All corundum crucibles were wrapped by carbon powder, which was designed to the CO reducing atmosphere for the samples. Finally, all samples were placed into the muffle furnace and sintered at 873 K for 5 h. After gradually natural cooling, all samples were collected for further measurement and analysis.

2.2 Measurements and Characterization

The X-ray diffraction (XRD) patterns data of the samples were collected by a Bruker D8 Discover X-ray diffractometer with Cu Kα radiation of λ = 0.154 18 nm ranging from 5° to 80°. The XRD data for Rietveld refinement were recorded by the same Bruker D8 Discover X-ray diffractometer in the range of 2θ from 5° to 130° in steps of 0.02° with a counting time of 4 s per step. The detailed crystal structure was analyzed by the general structure analysis system (GSAS) software[40]. A field emission scanning electron microscope (SEM) (FESEM, FEI Quanta 450 FEG) equipped with the energy-dispersive X-ray spectroscopy (EDS) was used to study the morphology of the as-prepared samples and the distribution of individual elements. The theoretical calculations including band structure and density of states were performed by the Cambridge Serial Total Energy Package (CASTEP) mode from Materials Studio software, which was conducted with the density functional theory (DFT) based on the first-principle calculation[41]. In the calculation process of exchange-correlation potential, the generalized gradient approximation (GGA) with the Perdew-Burke-Ernzerhof (PBE) functional was employed[42]. The K-$3p^64s^1$, Ba-$5p^65d^{10}6s^2$, P-$3s^23p^3$, O-$2s^22p^4$, F-$2s^22p^5$ were considered as the valence electrons. The plane-wave energy cut-off was determined to be 940 eV. The Monkhorst-Pack scheme for the host was chosen as 2×2×3 in the Brillouin zone. Diffuse reflection spectra of the samples were measured by a dual beam ultraviolet-visible spectrophotometer (TU-1901, PERSEE) coupled with the accessory of an integrating sphere and referred with the powder material $BaSO_4$. Photoluminescence excitation (PLE) spectra and the photoluminescence (PL) spectra of the phosphors were carried on a fluorescence spectrometer (FS5, Edinburgh Instruments), which is equipped with 150 W xenon arc lamp. The slit widths of the fluorescence spectrometer in the excitation and

emission spectra measurements were set to be 0.5 nm. Temperature-dependent PL spectra of the representative phosphor were also investigated by the FS5 fluorescence spectrometer, along with a self-regulating temperature-control accessory. The fluorescence lifetime and IQE were measured using a steady and transient state fluorescence spectrometer (JOBIN YVON FL-1057) by monitoring the given emission form the samples under the 370 nm pulsed laser excitation. The external quantum efficiency (EQE) was performed on an absolute PL quantum yield measurement system (C9920-02, HAMAMATSU). All measurements were conducted under room temperature.

3　Results and Discussion

3.1　Crystal Structure and Morphology

Fig. 1(a) exhibits the powder XRD patterns of KBPOF: xEu^{2+} (x=0–0.10) samples. It is observed that all diffraction peaks of KBPOF: xEu^{2+} match well with those of the calculated data of KBPOF crystal, demonstrating that Eu^{2+} ions at the current level of doping concentration are incorporated into the host lattice without any impurity phase[32]. As shown in Fig. 1(b), one can see that the main peak locating at around 2θ=30° shifts to the direction of higher angle with the increasing concentration of Eu^{2+} ions, suggesting that the doping Eu^{2+} ions substituting for the larger cations in KBPOF host cause the reduction of d value according to Bragg's law of $2d\sin\theta = n\lambda$[43]. Thus, the 2θ angles get gradually enlarged with the incremental concentration of Eu^{2+} ions. Furthermore, the crystallographic occupancies of the doping Eu^{2+} ions can be qualitatively identified by the respective radius difference of the cations in KBPOF:Eu^{2+} phosphor, which is expressed as follows[31]:

$$D_r = \frac{R_m(\mathrm{CN}) - R_d(\mathrm{CN})}{R_m(\mathrm{CN})} \times 100\%, \qquad (1)$$

herein, R_m(CN) and R_d(CN) represent the ionic radii of the potentially substituted cations (K$^+$ and Ba^{2+}) in the host and dopant ion (Eu^{2+}), respectively. CN means the coordinated number of cation in KBPOF:Eu^{2+}, and D_r denotes the calculated percentage. Given that the radii of 8-coordinated K$^+$/Eu^{2+} and 10-coodinated Ba^{2+}/Eu^{2+} cations are 0.151/0.125 nm and 0.152/0.135 nm, the corresponding values of D_r based on Eq. (1) are calculated to be 17.2% and 11.2%, respectively[44]. If the value of calculated percentage is less than 30%, the doped ions tend to occupy the corresponding crystallographic cation sites in the host lattice[31]. Therefore, it is reasonable to infer that the doped Eu^{2+} ions are likely to occupy the 8-/10-coordinated K$^+$/Ba^{2+} sites in the KBOPF host. In order to verify this inference, Rietveld refinement was conducted to obtain the detailed crystallographic information of the representative KBPOF:0.03Eu^{2+} phosphor, as depicted in Fig. 1(c), Tab. 1 and Tab. 2. By taking the crystal structure of KBPOF as the starting model for the structural refinement of KBPOF:0.03Eu^{2+}, the refinement result demonstrates that all simulated XRD peaks correspond well with those of experimental data. As shown in Tab. 1, the KBPOF:Eu^{2+} phosphor crystallizes in a tetragonal crystal system with space group of $I4/mcm$ (140), and the unit cell parameters (a=b=

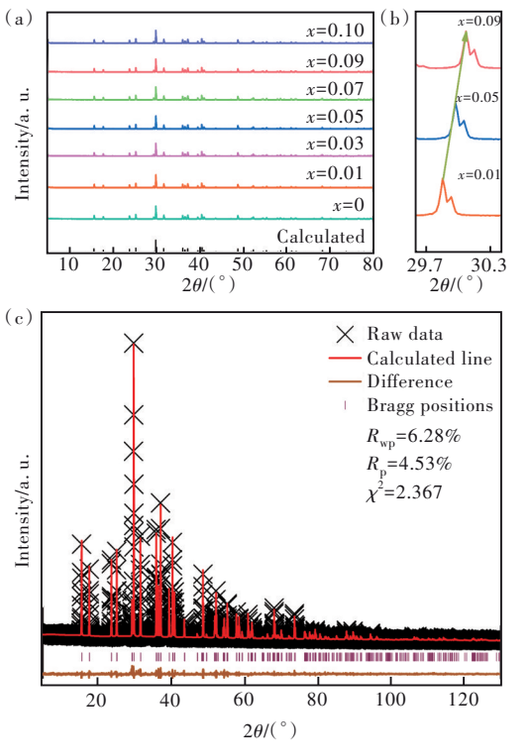

Fig.1　(a) XRD patterns of KBPOF: xEu^{2+} (x=0–0.10) samples. (b) The enlarged view of main peak for the typical KBPOF: xEu^{2+} phosphors. (c) Rietveld refinement of XRD data of the representative KBPOF: 0.03Eu^{2+} phosphor.

Tab. 1 XRD refinement parameters of the representative KBPOF:0.03Eu^{2+} phosphor

Formula	Crystal system	Profile range/(°)	Radiation type; λ/nm	Temperature/K	Space group (*Z*)	*a*/nm
KBPOF:0.03Eu^{2+}	Tetragonal	5–130	X-ray; 0.154 18	298	*I*4/*mcm* (140) (4)	0.701 4(3)
c/nm	Unit cell volume *V*/nm^3		Profile *R*-factor, R_p/%		Weighted profile *R*-factor, R_{wp}/%	χ^2
1.127 1(6)	0.554 5(6)		6.28		4.53	2.367

Tab. 2 Refinement results of the atomic coordinates of KBPOF:0.03Eu^{2+} phosphor

Atom	Occupancy	*x*/*a*	*y*/*b*	*z*/*c*	*U*
Ba1	0.981 2	1/2	1/2	3/4	0.027 6(2)
K1	0.988 8	0.176 56(8)	0.323 44(8)	1/2	0.020 1(8)
P1	1.000 0	1/2	0	1/4	0.021 5(6)
F1	1.000 0	1/2	1/2	1/2	0.017 3(8)
O1	1.000 0	0.374 04(19)	0.125 96(19)	0.329 32(18)	0.021 1(9)
Eu(1)	0.018 8	1/2	1/2	3/4	0.027 6(2)
Eu(2)	0.011 2	0.176 56(8)	0.323 44(8)	1/2	0.020 1(8)

0.701 4(3) nm, *c*=1.127 1(6) nm and *V*=0.554 5(6) nm^3) are slightly smaller than the reported crystallographic parameters of KBPOF crystal (*a*=*b*=0.702 6(4) nm, *c*=1.127 9(4) nm and *V*=0.556 8(6) nm^3) due to the shrinkage of crystal lattice resulting from the substitution of larger cations by the smaller Eu^{2+} ions[32]. During the process of Rietveld refinement, the sums of occupations, *viz.*, occ(Ba) + occ(Eu) and occ(K) + occ(Eu), are restricted to be 1. The final refinement result demonstrates that Ba^{2+} and K^+ cation sites are both occupied by the doped Eu^{2+} ions with the ratios of 0.981 2/0.018 8 (Ba/Eu) and 0.988 8/0.011 2 (K/Eu), respectively, which are supported by the convincingly residual factors R_p=6.28%, R_{wp}=4.53%, and χ^2=2.367. Taking into account both of Rietveld refinement analysis and similar cationic radii, it is reasonably confirmed that Eu^{2+} ions will occupy Ba^{2+} and K^+ sites in the KBPOF:Eu^{2+} host lattice.

Fig. 2(a) depicts the crystal structure of KBPOF and classic perovskite $CaTiO_3$ compound for comparison. For the crystal structure of KBPOF, the F-centered $[FK_4Ba_2]$ octahedra interconnects by sharing K and Ba atoms to make up its three-dimensional perovskite-type structure with the $[PO_4]$ tetrahedra residing in the space of adjacent $[FK_4Ba_2]$ octahedra, which is in analogy with the crystal structure of $CaTiO_3$. As depicted in Fig. 2(b), they share the similar structural features, *viz.*, the position site of $[TiO_6]$ octahedron is occupied by $[FK_4Ba_2]$ octahedron in the cubic perovskite structure, and the position of Ca^{2+} cation is similar to that of $[PO_4]$ tetrahedron. The $[KO_6F_2]$ and $[BaO_8F_2]$ polyhedra presented in Fig. 2(c) further demonstrate the detailed local coordination environments of corresponding cations with different bond lengths ($d_{K\text{-}O1}$=0.274 9(0) nm, $d_{K\text{-}O2}$=0.288 9(8) nm, $d_{K\text{-}F}$=0.258 9(2) nm; $d_{Ba\text{-}O}$=0.291 3(9) nm, $d_{Ba\text{-}F}$=0.281 9(8) nm). Thus, two different Eu^{2+} luminescence centers which occupy the K^+ and Ba^{2+} cation sites of the $[KO_8F_2]$ and $[BaO_6F_2]$ polyhedra tend to exhibit the distinct PL behaviors, being generally responsible for the intense narrow-band blue-emitting luminescence in our perovskite-type KBPOF:Eu^{2+} phosphor as discussed below.

Since the morphology and crystallinity of the phosphor have the significant influence on its fluorescence performance and the luminous efficiency of fabricated devices, the SEM measurement of the as-prepared KBPOF:0.03Eu^{2+} phosphor was conducted and its photograph is displayed in Fig. 3(a). It is observed that the phosphor composes of distinctly irregular particles with slight agglomeration owing to the high-temperature solid-state synthesis process[45].

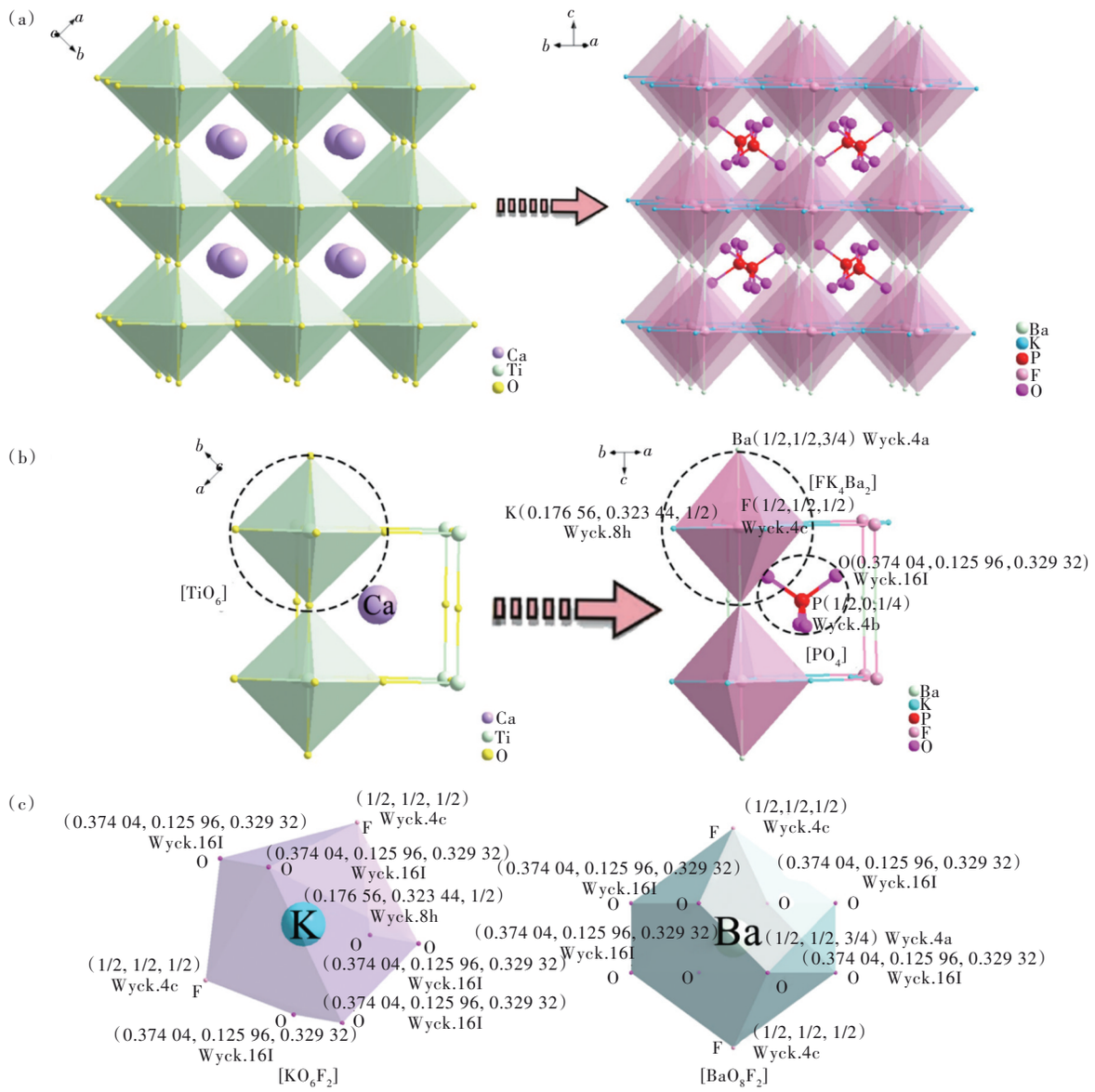

Fig.2　(a)The crystal structure of $CaTiO_3$ and KBPOF host. (b)The comparation of $CaTiO_3$ and KBPOF host units. (c)Coordination environments of K^+ and Ba^{2+}cations.

The sizes of ununiform particles basically distribute ranging from 1 μm to 7 μm with the average size of 3.15 μm, which is attributed to the long calcination time (Fig. 3(b)). For further investigation on the distribution of individual element in the KBPOF:Eu^{2+} phosphor, the selected particle was utilized for EDS mapping measurement as shown in Fig. 3(c). It is found that all of the elements are uniformly distributed and accumulated in the whole particle. As displayed in Fig. 3(d), The measured atomic ratio of K:Ba:P:O:F:Eu is determined to be 19.89:9.37:10.03:49.47:11.16:0.08, being close to the nominal ratio in the chemical formula KBPOF:0.03Eu^{2+} and thus indicating the phase formation of our perovskite-type phosphor.

3.2　Band Structure and Optical Band Gap

Investigation on the band structure of KBPOF and density of electronic states (DOS) can provide further insight into the nature of intrinsic electronic structure. Fig. 4(a) and (b) exhibit the band structure as well as total and partial density of states (TDOS and PDOS) of KBPOF host by using the total-energy code CASTEP based on the first-principle calculation with DFT[41]. As shown in Fig. 4(a), the bottom of the conduction band locating at G point and the top of the valence band locating at P point in

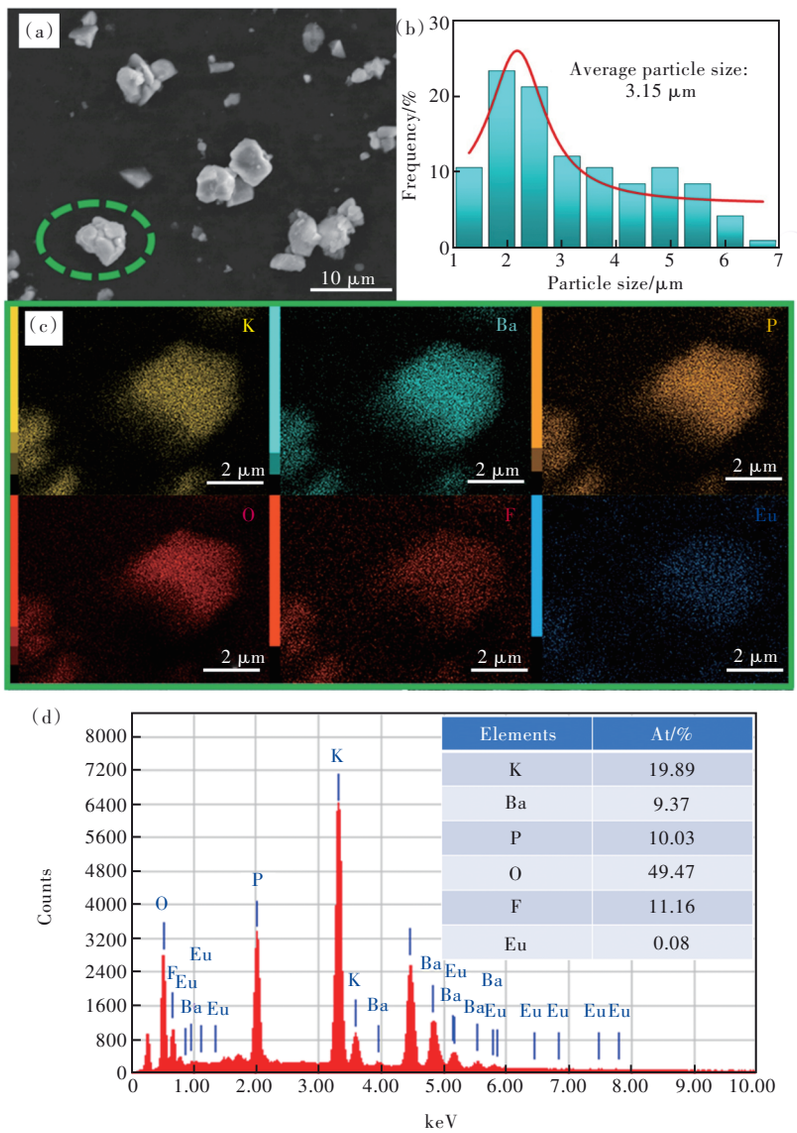

Fig.3 (a)SEM image of KBPOF:0.03Eu^{2+}. (b)Histogram of particle size distribution of KBPOF:0.03Eu^{2+} phosphor. (c)EDS elemental mapping images of corresponding elements. (d)The measured EDS result of KBPOF:0.03Eu^{2+}. The inset is the atoms percentage in the KBPOF:0.03Eu^{2+}.

the Brillouin zone clearly demonstrate that the KBPOF host exhibits the indirect bandgap nature with the large value of 5.035 eV, being beneficial for realizing the efficient down-conversion luminescence in the corresponding phosphor since such a large bandgap can favorably accommodate the ground and excited states of the doping Eu^{2+} ions in the KBPOF host lattice[26]. As depicted in Fig. 4(b), the energy distribution of PDOS projected onto K, Ba, P, O, and F contributions in the valence band is divided into the three portions, namely, the low-energy region (from −30 eV to −25 eV), the middle-energy region (from −25 eV to −10 eV), and the high-energy region (from −10 eV to 0 eV). One can see that the low-energy region is attributable to the contributions of K-4s and Ba-6s orbitals. The K-3p, Ba-5p, P-3s, P-3p, O-2s, and F-2s orbitals are responsible for the middle-energy region of valence band, in which the O-2s orbital hybridizes with the P-3s and P-3p orbitals owing to their superposition, thereby indicating the formation of [PO_4] tetrahedra in the crystal structure of KBPOF host. The high-energy region near the Fermi energy level is dominated by O-2p and F-2p orbitals with bits of P-3s, P-3p and O-2s orbitals. Among them, the overlap between O-2p and P-3p orbitals demonstrates that the O-2p orbital hybridizes

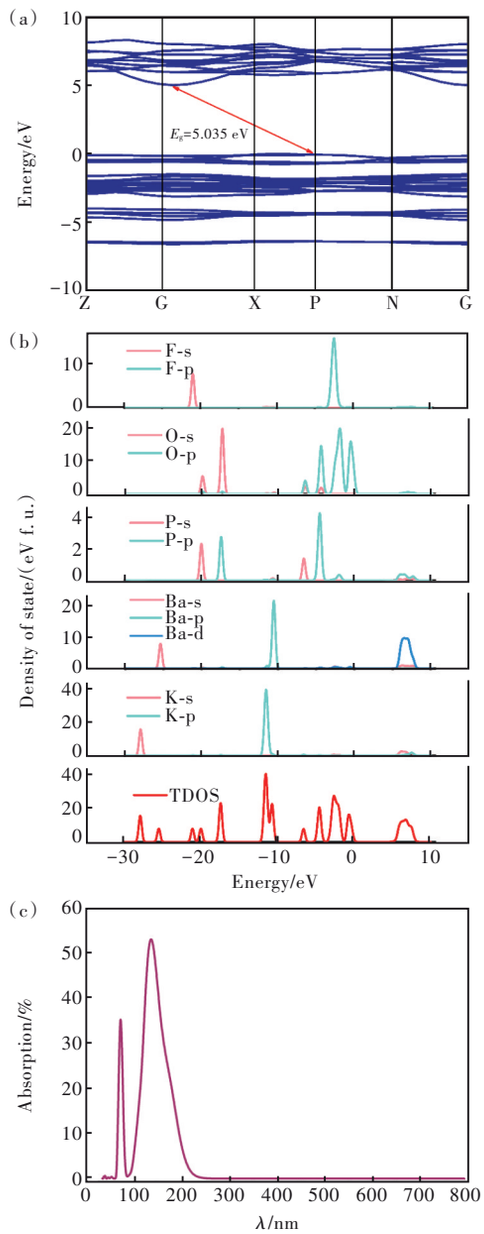

Fig.4　Calculated band structure(a), DOS(b), and absorption spectrum(c) of KBPOF host based on DFT.

with the P-3p orbital to form P—O bond in the $[PO_4]$ tetrahedra. The energy of the bottom of conduction band ranging from 0 to10 eV is ascribed to the dominated contribution of Ba-5d orbital. The theoretical optical absorption spectrum was also calculated and exhibited in Fig. 4(c). It is observed that the absorption region mainly locates in the range of 70–220 nm. Given that the absorption band of Eu^{2+} in the KBPOF: Eu^{2+} phosphor is located at the near-UV region as depicted in the following Fig. 6, the calculated absorption region shown in Fig. 4(c) reflects the intrinsic absorption of the KBPOF host.

Fig. 5(a) shows the diffuse reflection spectra of KBPOF host and KBPOF: 0.03Eu^{2+} phosphor. For the pure KBPOF host, the reflectance starts from 190 nm and it drops until up to around 210 nm. The reflectance then increases and gradually stretches in the range of 210–800 nm. Among them, the absorption region in the range of 190–400 nm is assigned to the absorption of KBPOF host. Nonetheless, it is observed that a distinct absorption region at 210–400 nm in the reflection curve of KBPOF: 0.03Eu^{2+} phosphor, which is attributed to the spin-allowed transition $4f^7$-$4f^65d^1$ of Eu^{2+} ion[31]. The experimental value of band gap can be calculated by the diffuse reflection spectra of KBPOF host based on the extrapolation method, which is guided by the following equations[46]:

$$\left[F(R)h\nu\right]^{1/2} = A\left(h\nu - E_g\right), \tag{2}$$

$$F(R) = \frac{(1-R)^2}{2R}, \tag{3}$$

where R and $F(R)$ are the reflectance coefficient and absorption coefficient, respectively. A is the absorption constant, and $h\nu$ represents the photon energy. E_g is the band gap. Fig. 5(b) exhibits the relationship

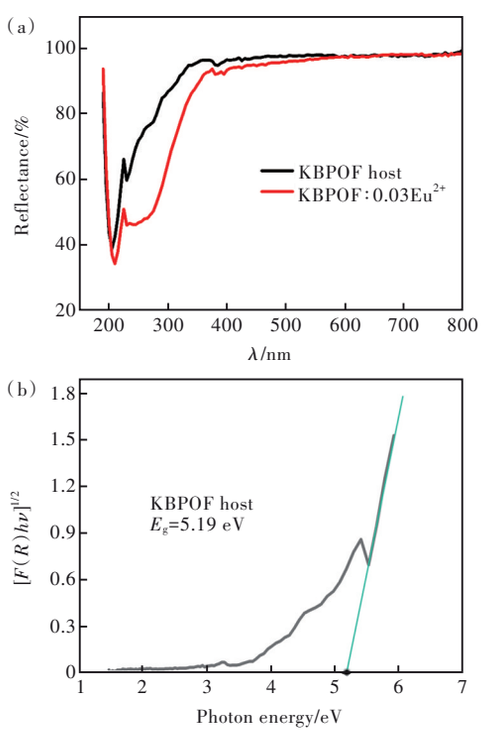

Fig.5　(a) Diffuse reflection spectra of undoped KBPOF host and KBPOF: 0.03Eu^{2+} phosphor. (b) The experimental band gap of KBPOF host.

of $[F(R)h\nu]^2$ on the photon energy for the KBPOF host. It is found that the tangent intersects the X-axis at a point with the value of 5.19 eV, which is larger than the value of the theoretical band gap (5.035 eV) based on the first-principle calculation. This discrepancy is attributed to the underestimate of insulators and semiconductors that derives from the simplification of the form of self-consistent band structure performed by the GGA module during the calculated process with DFT[47]. Therefore, the value of experimental band gap is usually larger than that of the theoretical band gap calculated by the first principle based on DFT.

3.3 PL Properties

Fig. 6 exhibits the PLE and PL spectra of KBPOF: $0.03Eu^{2+}$ phosphor under room temperature. Upon the excitation of 365 nm, the KBPOF: Eu^{2+} phosphor displays the intense blue emission band peaking at 432 nm with narrow FWHM of 43 nm, which is attributed to the characteristic electric-dipole spin-allowed $4f^65d^1$-$4f^7$ transition of Eu^{2+}[31]. Tab. 3 exhibits the narrow FWHM of KBPOF: Eu^{2+} in comparison with that of some recently reported blue-emitting phosphors, such as $Ca_8La_2(PO_4)_6O_2$: Ce^{3+} (FWHM=100 nm), $NaCaBO_3$: Ce^{3+} (FWHM=75 nm), and $Cs_4Mg_3CaF_{12}$: Eu^{2+} (FWHM=119 nm), demonstrating its favorable color saturation of our developed narrow-band blue-emitting phosphor. Furthermore, one can see that the shape of the PL spectrum is slightly asymmetric, which implies this spectrum curve could be superimposed by multiple PL spectra curves deriving from the distinct luminescence centers. As shown in Fig. 6, by utilizing the Gaussian fitting method, the PL spectrum is reasonably decomposed into two sub-bands with peaks at 410 nm and 433 nm, corresponding to two distinct Eu^{2+} luminescence centers which is consistent with the occupancy result obtained from the Rietveld refinement as discussed above. Normally, the fluorescence feature of Eu^{2+} luminescence center is closely related to its local coordination environment of Eu^{2+} ions in the phosphor. In the perovskite-type KBPOF host lattice, there are two kinds of large cations surrounded by different local coordination environments, in which Ba^{2+} coordinates with eight O and

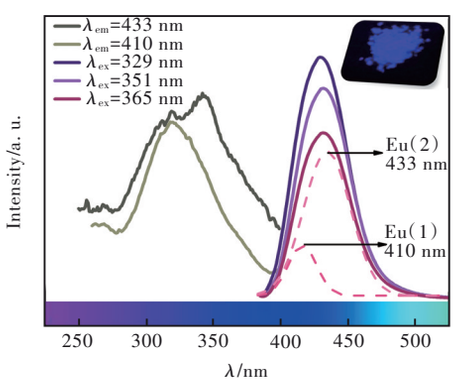

Fig.6 PLE and PL spectra of KBPOF: $0.03Eu^{2+}$ phosphor. The PL spectrum excited by 365 nm is separated into two sub-peaks with the maximum at 410 nm and 433 nm by the Gaussian fitting method. The inset shows the digital photograph of the corresponding phosphor under 365 nm excitation.

Tab. 3 Comparison of the title KBPOF: Eu^{2+} phosphor with some reported blue-emitting phosphors

Phosphor	FWHM/nm	Excitation range/nm	Emission range/nm	Thermal stability	IQE/%	EQE/%
$Cs_4Mg_3CaF_{12}$: Eu^{2+}[26]	119	300–400	400–600	$I_{473\ K}/I_{298\ K}$=80%	64.0	—
$K_{1.6}Al_{11}O_{17+\delta}$: Eu^{2+}[35]	70	200–450	400–600	$I_{373\ K}/I_{298\ K}$=99%	97.0	62
$Na_3Sc_2(PO_4)_3$: Eu^{2+}[36]	50	250–430	400–550	$I_{473\ K}/I_{298\ K}$=100%	74.0	—
$Ba_9Lu_2Si_6O_{24}$: Eu^{2+}[37]	50	250–450	450–600	$I_{473\ K}/I_{298\ K}$=18%	68.0	45
$KBaYSi_2O_7$: Eu^{2+}[38]	58	300–450	420–500	$I_{473\ K}/I_{298\ K}$=10%	35.0	—
$Ba_2Y_5B_5O_{17}$: Bi^{3+}[39]	49	250–400	385–500	$I_{473\ K}/I_{298\ K}$ < 50%	46.0	—
$Ba_2Lu_5B_5O_{17}$: Ce^{3+}[48]	112	250–390	400–550	$I_{423\ K}/I_{298\ K}$=56%	92.0	—
$NaCaBO_3$: Ce^{3+}[49]	75	250–400	400–500	$I_{453\ K}/I_{298\ K}$=40%	75.0	—
$Ca_8La_2(PO_4)_6O_2$: Ce^{3+}[50]	100	250–400	400–600	—	59.0	—
$Sr_3MgSi_2O_8$: Eu^{2+}[51]	62	200–400	400–500	$I_{473\ K}/I_{298\ K}$ < 60%	—	—
$BaMgAl_{10}O_{17}$: Eu^{2+}[52]	51	200–400	400–550	$I_{473\ K}/I_{298\ K}$=95%	89.0	35
KBPOF: Eu^{2+}	42	300–400	400–500	$I_{493\ K}/I_{298\ K}$=64%	72.8	

two F atoms to establish the $[BaO_8F_2]$ polyhedron, and K^+ coordinates with six O and two F atoms to form the $[KO_6F_2]$ polyhedron. In order to understand the relationship between the local coordination environment and spectral properties of KBPOF: Eu^{2+} phosphor, the following equation based on the Van Uitert theory can be used as a reference[31]:

$$E = Q\left[1 - \left(\frac{V}{4}\right)^{1/V} 10^{-nE_a r/80}\right], \quad (4)$$

$$E\lambda = 10^7, \quad (5)$$

herein, E is the peak position of the phosphor in the PL spectra (cm^{-1}); Q refers to the lowest position of edge band of 5d energy level for crystal field splitting (34 000 cm^{-1} for Eu^{2+} generally), and V represents the valence state of doped Eu^{2+} ions (V=2); n and r are the coordinated number and the radius of the possible cationic occupancy replaced by doped ions (n=8 for K^+, n=10 for Ba^{2+}; r_{K^+}=0.151 nm; $r_{Ba^{2+}}$=0.152 nm); E_a stands for the electronic affinity of anion in the host. λ is the emission wavelength of the phosphor. According to Eqs. (4) and (5), it is concluded that the coordinated number n is positively correlated with the emission peak position E, while the emission wavelength λ is inversely proportional to the emission peak position E. Therefore, the Eu^{2+} ion substituting for ten-coordinated Ba^{2+} site forms the Eu(1) luminescence center with the emission wavelength of 410 nm, whereas that occupying eight-coordinated K site forms the Eu(2) luminescence center with the emission wavelength of 433 nm. It is also observed from Fig. 6 that two PLE spectra under monitoring at 410 nm and 433 nm exhibit the distinct shape profiles and different excitation peak positions (329 nm and 351 nm), convincingly demonstrating that the existence of distinct Eu(1) and Eu(2) luminescence centers in the perovskite-type KBPOF: Eu^{2+} phosphor. The corresponding PL spectra of KBPOF: Eu^{2+} excited by 329 nm and 351 nm also display different emission bands with different peak positions, thereby confirming the distinct luminescence features of Eu(1) and Eu(2) in the KBPOF: Eu^{2+} phosphor. Additionally, it is observed that the PLE spectrum of Eu(2) center partly covers with the PL spectrum of Eu(1) center in the wavelength range of 380–400 nm (Fig. 6), thus indicating that the energy transfer process is likely to occur between Eu(1) and Eu(2) centers in our perovskite-type phosphor.

3.4 Energy Transfer Process from Eu(1) to Eu(2)

The investigation in the fluorescence decay dynamics of different Eu luminescence centers can provide further evidence for confirming their intrinsic energy transfer process. Fig. 7(a) and (b) present the fluorescence decay curves of KBPOF: xEu^{2+} phosphors (x=0.01–0.10) for Eu(1) and Eu(2) luminescence centers. The decay curves under monitoring at 410 nm and 433 nm accord with the double-exponential decay profiles, which can be well fitted by the following formula[26]:

$$I_t = I_0 + A_1\exp(-t/\tau_1) + A_2\exp(-t/\tau_1), \quad (6)$$

where I_t and I_0 represent the emission intensity of corresponding phosphor at time t and 0, respectively. A_1 as well as A_2 refers to the constant. τ_1 and τ_2 denote the rapid and slow lifetime of the double-exponential components, respectively. The average luminescence lifetime (τ^*) can be calculated by the following equation[26]:

$$\tau^* = \frac{A_1^2\tau_1^2 + A_2^2\tau_2^2}{A_1\tau_1 + A_2\tau_2}, \quad (7)$$

based on Eq. (7), the average luminescence lifetime for Eu(1) luminescence center monitored at 410 nm is calculated to be 1.84, 1.57, 1.32, 1.16, 1.08, 0.79 μs, and that for Eu(2) luminescence center is calculated to be 0.89, 0.96, 1.02, 1.09, 1.14, 1.16 μs with x=0.01–0.10. Thus, it can be concluded that the luminescence lifetime of Eu(1) center sharply decreases with the incremental doping content of Eu^{2+}, while that of Eu(2) center exhibits the increasing tendency, evidently confirming the existence of energy transfer process from Eu(1) to Eu(2) in our perovskite-type KBPOF: Eu^{2+} phosphors. The whole energy transfer process between Eu(1) and Eu(2) can be intuitively understood by a schematic configuration coordination model, as shown in Fig. 7(c). As discussed above, the Gaussian emission band peaking at 410 nm originates from the Eu

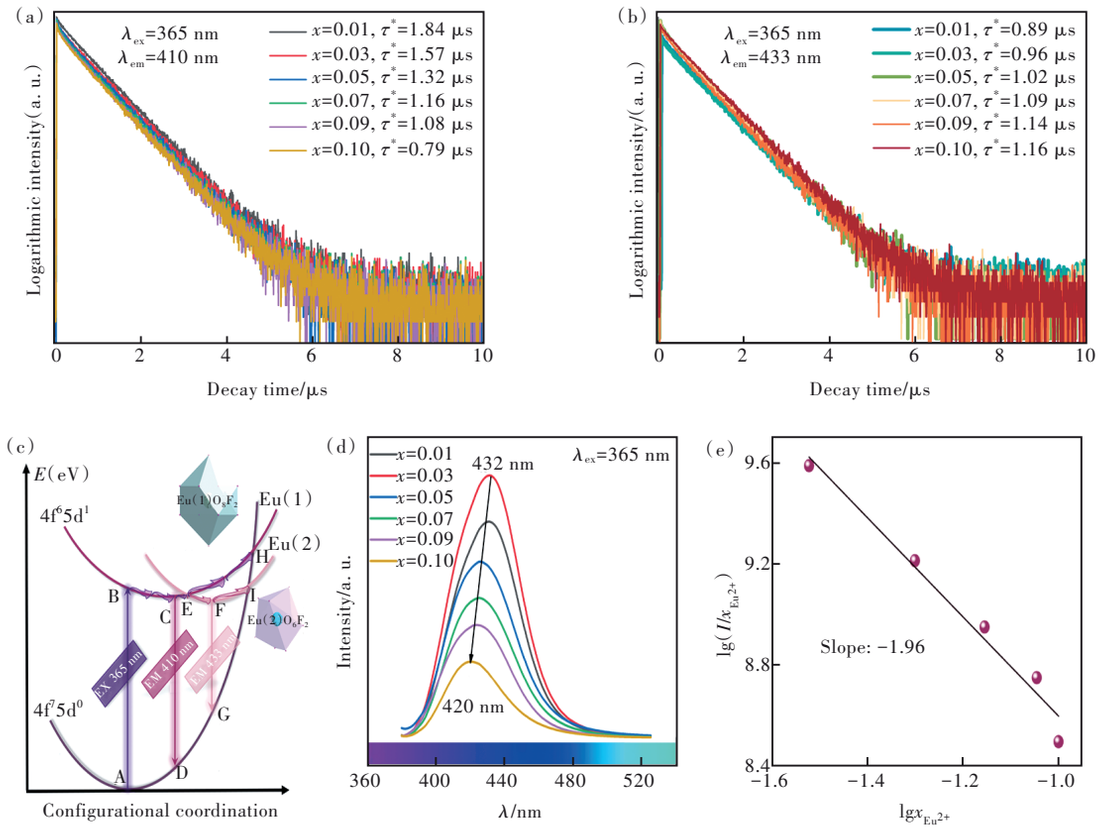

Fig.7 PL decay curves of KBPOF:xEu^{2+}(x=0.01−0.10) phosphor for Eu(1)(a) and Eu(2)(b). Two insets in (a) and (b) present the respective average lifetime value with the corresponding Eu^{2+} doping concentration. (c)Schematic illustration of the configurational coordination diagram of Eu^{2+} in the KBPOF:Eu^{2+} phosphor. (d)PL spectra of KBPOF:xEu^{2+} phosphors (x=0.01−0.10). (e)The linear fitting relationship between $\lg x_{Eu^{2+}}$ and $\lg(1/x_{Eu^{2+}})$.

(1) center that occupies ten-coordinated Ba^{2+} site to form the [Eu (1) O_8F_2] polyhedron, while another Gaussian emission band peaking at 433 nm derives from the Eu(2) center which substitutes the eight-coordinated K site to form the [Eu(2) O_6F_2] polyhedron. Under the excitation of 365 nm, the electrons of Eu(1) center transit from the $4f^7$ ground state to the $4f^65d^1$ excited state, and then return to the ground state along with the shorter emission wavelength of 410 nm. On the other hand, these excited electrons in the $4f^65d^1$ excited state of Eu(1) can also transfer to the lower $4f^65d^1$ excited state of Eu(2) through the point N. Then, the electrons return back to the $4f^7$ ground state by overcoming the energy barrier, exhibiting the longer emission with the wavelength of 433 nm. Based on the above electron transition process, the energy transfer is reasonably expected to occur between Eu(1) donor and Eu(2) acceptor in the perovskite-type KBPOF: Eu^{2+} phosphors.

Fig. 7(d) exhibits the concentration-dependent PL spectra of the KBPOF: xEu^{2+} (x=0.01−0.10) phosphor upon the excitation of 365 nm. One can see that all of the spectral profiles are asymmetric along with the long trailing in the long-wavelength side. The FWHM value of PL spectrum increases from 43 nm to 48 nm with increasing of Eu^{2+} doping concentration. The corresponding emission peak position also shows the blue-shift behavior ranging from 432 nm to 420 nm, which is assigned to the changing strength of crystal field splitting relying on the doping concentration of Eu^{2+} ion. The crystal splitting effect can be qualitatively described by the following equation[31]:

$$D_q = \frac{Ze^2r^4}{6R^5}, \tag{8}$$

where Z and e stand for the anion charge and electron charge, respectively; r is the radius of the d wave function; R represents the bond length of the cation and its coordinated ions; D_q is energy level separation.

When the smaller Eu^{2+} ion substitutes the larger Ba^{2+} and K^+ cations in the perovskite-type KBPOF host, the bond lengths of corresponding coordination polyhedra tend to get elongate. According to Eq. (8), it is concluded that the crystal field splitting D_q is proportional to $1/R^5$. The longer bond length can cause the smaller D_q of Eu^{2+} 5d energy level. Therefore, the blue-shift behavior of emission peak position occurs in the KBPOF: Eu^{2+} phosphors. In addition, as also shown in Fig. 7(d), the PL intensity increases when the Eu^{2+} concentration changes from 0.01 to 0.03 and then it gradually decreases, which is ascribed to the concentration quenching effect of Eu^{2+} in the KBPOF: Eu^{2+} phosphor and can be determined by the critical distance(R_c) of the neighboring Eu^{2+} ions[52]:

$$R_c \approx 2\left(\frac{3V}{4\pi X_c N}\right)^{1/3}, \tag{9}$$

here, V and N represent the cell volume of the host (V=0.556 8(6) nm^3) and the potential cation number replaced by the dopant Eu^{2+} (N=4), respectively[33]; X_c is the critical concentration of Eu^{2+} dopant in the KBPOF: Eu^{2+} phosphor (X_c=0.03). Based on Eq. (9), the value of critical distance(R_c) is calculated to be 2.069 nm. It is widely recognized that the electric multipole interaction between the adjacent Eu^{2+} ions is responsible for the energy transfer process and resulting concentration quenching effect when the critical distance R_c is greater than 0.5 nm. Thus, the following equations are further given in order to determine the specific type of electric multipole interaction in the KBPOF: Eu^{2+} phosphor[53]:

$$\frac{I}{x} = k\left[1 + \beta(x)^{\theta/3}\right]^{-1}, \tag{10}$$

$$\lg\frac{I}{x} = K' - \frac{\theta}{3}\lg x\left(K' = \lg k - \frac{\theta}{3}\lg\beta\right), \tag{11}$$

where I stands for the PL intensity of the corresponding Eu^{2+} concentration(x) which starts from its critical concentration (x=0.03). k and β are the constants with the same excitation condition for the KBPOF: Eu^{2+} phosphor. θ is a symbol to denote the type of the electric multipolar interaction, particularly, θ=6, 8, or 10 corresponding to the dipole-dipole, dipole-quadrupole, or quadrupole-quadrupole interaction[53]. The dependent relationship between $\lg x_{Eu^{2+}}$ and $\lg(I/x_{Eu^{2+}})$ obtained from Eq. (11) is given in Fig. 7(e). Therefore, the θ value is calculated to be 5.88, indicating that the electric dipole-dipole interaction involves in the energy transfer process and dominates the concentration quenching effect in our phosphor system.

3.5 Thermal Stability and Quantum Efficiency

The thermal stability is commonly utilized to evaluate the application potential of phosphor which is used in the LED device applicable for LCD backlighting field. In 2021, Leng *et al.* firstly reported the zero-thermal-quenching property of the perovskite-type KBPOF: Eu^{2+} phosphor in the increasing temperature range of 298−393 K, which was ascribed to the large band gap, high lattice and high symmetry of the perovskite-type KBPOF host[34]. In order to check this inference, the temperature-dependent PL spectra of the representative KBPOF: $0.03Eu^{2+}$ phosphor are displayed in Fig. 8(a) and (b). It is observed that the PL intensity obviously decreases with the temperature increasing from 293 K to 493 K, attributing to the temperature quenching effect. It is also evidenced that the respective PL intensity of two distinct Eu^{2+} luminescence centers decreases with the increasing temperature, further disagreeing with the aforementioned conclusion referring to the remarkable zero-thermal-quenching feature of KBPOF: Eu^{2+} as previously reported by Leng *et al*[34]. The whole temperature quenching process for different Eu^{2+} luminescence centers is reasonably elucidated according to the schematic configuration coordination model (Fig. 7(c)). In general, the thermal quenching process can be interpreted as the phonon-electron mutual effect, which is usually strengthened with increasing of the temperature. At room temperature, the electrons in the respective lowest energy level of Eu(1) and Eu(2) $4f^6 5d^1$ excited state (C point and F point) will return to the $4f^7 5d^0$ ground state (D point and G point), resulting in the blue luminescence in the perovskite-type KBPOF: Eu^{2+} phosphor. Nonetheless, as the temperature increases, the electrons will surmount the respective energy level difference and transport to the higher energy

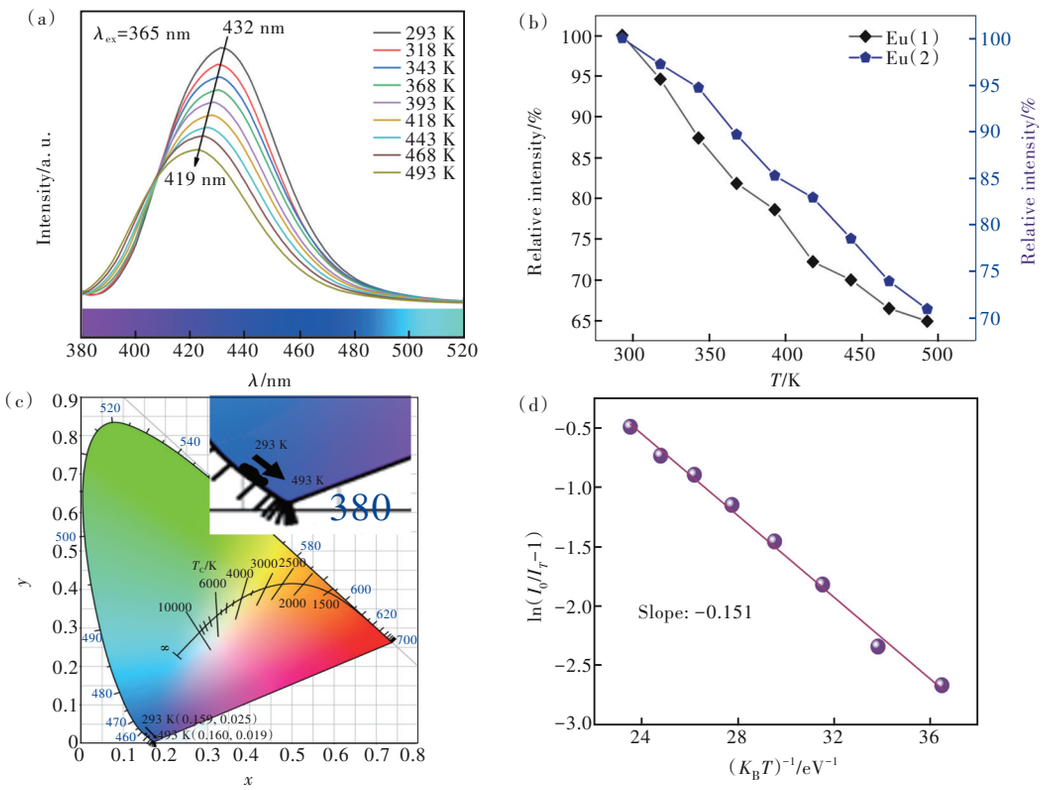

Fig.8 (a)PL spectra of KBPOF:0.03Eu^{2+} phosphor with different temperature under monitoring at 365 nm. (b)The comparation of PL intensity of Eu(1) and Eu(2) centers for KBPOF:0.03Eu^{2+} phosphor with the increasing temperature. (c)The detailed CIE chromaticity coordinates of KBPOF:0.03Eu^{2+} phosphor with the increasing temperature(K). (d)The linear fitting relationship between $\ln(I_0/I_T-1)$ and $1/(K_BT)$ according to the Arrhenius equation.

$4f^65d^1$ excited state through thermal phonon assisting (this process is denoted as C-H curve and F-I curve), which means that the electrons are more likely to cross the respective intersection point (H point and I point) between the $4f^65d^1$ and $4f^75d^0$ states and eventually return to the $4f^75d^0$ ground state nonradiatively. As a consequence, the temperature quenching behavior is reasonably observed in the KBPOF:Eu^{2+} phosphor with increasing temperature. The PL intensity of phosphor remains 77%/64% of the initial intensity when the temperature increases up to 393 K/493 K, which is inferior to the representative blue-emitting phosphors such as zero-thermal $K_{1.6}Al_{11}O_{17+\delta}$:$Eu^{2+}$[35] and $Na_3Sc_2(PO_4)_3$:Eu^{2+}[36] phosphors as well as the commercial BAM:Eu^{2+}[52] phosphor, but significantly superior to some other previously reported phosphors as listed in Tab. 3. As presented in Fig. 8(a), it is observed that the emission peak position slightly shifts from 432 nm to 419 nm with increasing of the temperature, which is consistent with the variation trend of their Commission Internationale de l'Eclairage(CIE) chromaticity coordinates with the increasing temperature of 293–493 K, varying from (0.159, 0.025) to (0.160, 0.019). The CIE chromaticity shift (ΔE) of the blue-emitting KBPOF:Eu^{2+} phosphor with the increasing temperature can be calculated by the following equation[54]:

$$\Delta E = \sqrt{(u_t' - u_0')^2 + (v_t' - v_0')^2 + (w_t' - w_0')^2}, \quad (12)$$

where $u'=4x/(3-2x+12y)$, $v'=9y/(3-2x+12y)$, as well as $w'=1-u'-v'$; 0 and t refer to the initial temperature (293 K) and increased temperature (493 K), respectively. Among them, u' and v' correspond to the color coordinates in the $u'v'$ uniform color space. x and y are the color coordinates in the CIE 1931 color space. Based on Eq. (12), the chromaticity shift(ΔE) of KBPOF:Eu^{2+} phosphor is calculated to be 20.6×10^{-3}, which demonstrates the better color stability of KBPOF:Eu^{2+} in comparison with that of BAM:Eu^{2+}(21.3×10^{-3}). Considering the activation energy(E) as the key parameter which reflects

the strength of electron-phonon interaction in the phosphor system, it can be calculated by the following Arrhenius equation[26]:

$$I_T = \frac{I_0}{1 + Ae^{(-E/K_B T)}}, \tag{13}$$

where I_0 and I_T stand for the PL intensity of the initial temperature and the heating temperature T. K_B is Boltzmann constant (8.62×10^{-5} eV·K^{-1}), A denotes a constant. According to Eq. (13), the dependent relationship of $\ln(I_0/I_T-1)$ *versus* $1/K_BT$ is depicted in Fig. 8(d). It can be found that the value of E is determined to be 0.151 eV. Theoretically, the activation energy (E) is closely related to the band gap between the lower energy level of Eu^{2+} 5d excited state and the bottom of the conduction band. The larger the value of activated energy, the better the thermal stability of the phosphor. Therefore, the thermal stability of KBPOF:Eu^{2+} is superior to some other representative blue-emitting phosphors as listed in Tab. 3.

Given that the η_{IQE} value is another crucial parameter to evaluate the photoelectric performance of phosphor applicable for LEDs, it can be obtained by the formula on the basis of Fig. 9[31]:

$$\eta_{IQE} = \frac{\int L_S}{\int E_R - \int E_S}, \tag{14}$$

where E_R and E_S are the spectrum of excitation light with and without the aim sample in the integrating sphere; L_S stands for the emission spectrum of the KBPOF:Eu^{2+} phosphor. Furthermore, the absorption efficiency (AE) η_{AE} and EQE (η_{EQE}) values of the representative phosphor are calculated using the following equations[55]:

$$\eta_{AE} = \frac{\int E_R - \int E_S}{\int E_R}, \tag{15}$$

$$\eta_{EQE} = \eta_{IQE} \times \eta_{AE}, \tag{16}$$

based on the Eqs. (14)-(16), the calculated η_{IQE}, η_{AE} and η_{EQE} values are determined to be 72.8%, 63.7% and 46.4%, which are also higher than some recently reported blue-emitting phosphors as exhibited in Tab. 3, thus demonstrating that the perovskite-type KBPOF:Eu^{2+} is a potential candidate as a efficiently narrow-band blue-emitting phosphor for the fabrication of LED devices applicable in the field of LCD backlighting.

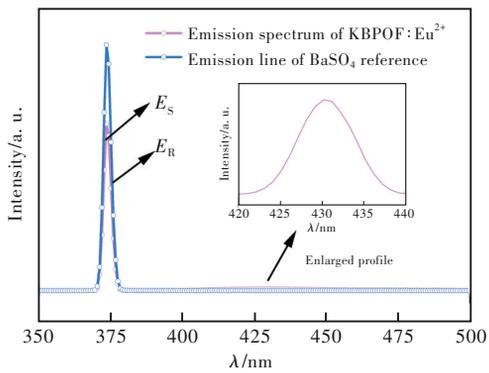

Fig.9　Excitation line of $BaSO_4$ and emission spectrum of the KBPOF:0.03Eu^{2+} sample. The inset is the magnification of the emission spectrum.

4　Conclusions

In summary, a novel narrow-band blue-emitting phosphor KBPOF:Eu^{2+} is successfully synthesized by the conventional solid-state reaction. The crystal structure of KBPOF is formed by the vertex-sharing [FK_4Ba_2] octahedron interconnected with each other together with [PO_4] tetrahedra. Under the excitation of near-UV light, KBPOF:Eu^{2+} displays a blue emission band peaking at 432 nm with narrow FWHM of 43 nm. Spectral analysis further confirms the existence of two distinct luminescence centers, *viz.*, Eu(1) and Eu(2), which occupy ten-coordinated Ba^{2+} site and eight-coordinated K^+ site in the perovskite-type KBPOF:Eu^{2+} phosphor. The energy transfer mechanism between Eu(1) and Eu(2) and PL properties of concentration-dependent and temperature-dependent spectra are also investigated in detail. The KBPOF:Eu^{2+} phosphor not only exhibits a suitable thermal stability (I_{493K}/I_{293K}=64%), but also displays the high η_{IQE} of 72.8% and η_{EQE} of 46.4%, surpassing some other reported blue-emitting phosphors. The present work not only demonstrates the potential of our developed perovskite-type KBPOF:Eu^{2+} phosphor, but also provides an avenue for exploring the novel phosphors inspired by the mineral-type structural prototypes.

Response Letter is available for this paper at: http://cjl.lightpublishing.cn/thesisDetails#10.37188/CJL.20220412.

References:

[1] 郑鹏, 丁国真, 解荣军. Ce^{3+}和Eu^{2+}掺杂荧光材料的光猝灭机理研究进展[J]. 发光学报, 2021, 42(10): 1447-1457.
ZHENG P, DING G Z, XIE R J. Research progress on optical quenching of Ce^{3+}- and Eu^{2+}-doped luminescent materials [J]. *Chin. J. Lumin.*, 2021, 42(10): 1447-1457. (in Chinese)

[2] LIAO H X, ZHAO M, ZHOU Y Y, *et al*. Polyhedron transformation toward stable narrow-band green phosphors for wide-color-gamut liquid crystal display [J]. *Adv. Funct. Mater.*, 2019, 29(30): 1901988-1-7.

[3] LIAO M, WANG Q, LIN Q M, *et al*. Na replaces Rb towards high-performance narrow-band green phosphors for back-light display applications [J]. *Adv. Opt. Mater.*, 2021, 9(17): 2100465-1-10.

[4] TOLHURST T M, SCHMIECHEN S, PUST P, *et al*. Electronic structure, bandgap, and thermal quenching of Sr-[Mg_3SiN_4]:Eu^{2+} in comparison to Sr[$LiAl_3N_4$]:Eu^{2+} [J]. *Adv. Opt. Mater.*, 2016, 4(4): 584-591.

[5] PUST P, WEILER V, HECHT C, *et al*. Narrow-band red-emitting Sr[$LiAl_3N_4$]:Eu^{2+} as a next-generation LED-phosphor material [J]. *Nat. Mater.*, 2014, 13(9): 891-896.

[6] PUST P, WOCHNIK A S, BAUMANN E, *et al*. Ca[$LiAl_3N_4$]:Eu^{2+}—a narrow-band red-emitting nitridolithoaluminate [J]. *Chem. Mater.*, 2014, 26(11): 3544-3549.

[7] ZHAO M, LIAO H X, NING L X, *et al*. Next-generation narrow-band green-emitting $RbLi(Li_3SiO_4)_2$:Eu^{2+} phosphor for backlight display application [J]. *Adv. Mater.*, 2018, 30(38): 1802489-1-7.

[8] DUTZLER D, SEIBALD M, BAUMANN D, *et al*. Alkali lithosilicates: renaissance of a reputable substance class with surprising luminescence properties [J]. *Angew. Chem. Int. Ed.*, 2018, 57(41): 13676-13680.

[9] LIAO H X, ZHAO M, MOLOKEEV M S, *et al*. Learning from a mineral structure toward an ultra-narrow-band blue-emitting silicate phosphor $RbNa_3(Li_3SiO_4)_4$:Eu^{2+} [J]. *Angew. Chem. Int. Ed.*, 2018, 57(36): 11728-11731.

[10] ZHU H M, LIN C C, LUO W Q, *et al*. Highly efficient non-rare-earth red emitting phosphor for warm white light-emitting diodes [J]. *Nat. Commun.*, 2014, 5(1): 4312-1-7.

[11] HUANG L, ZHU Y W, ZHANG X J, *et al*. HF-free hydrothermal route for synthesis of highly efficient narrow-band red emitting phosphor $K_2Si_{1-x}F_6$:xMn^{4+} for warm white light-emitting diodes [J]. *Chem. Mater.*, 2016, 28(5): 1495-1502.

[12] YI X D, LI R F, ZHU H M, *et al*. K_2NaAlF_6:Mn^{4+} red phosphor: room-temperature synthesis and electronic/vibronic structures [J]. *J. Mater. Chem.* C, 2018, 6(8): 2069-2076.

[13] DENG T T, SONG E H, SUN J, *et al*. The design and preparation of the thermally stable, Mn^{4+} ion activated, narrow band, red emitting fluoride Na_3GaF_6:Mn^{4+} for warm WLED applications [J]. *J. Mater. Chem.* C, 2017, 5(11): 2910-2918.

[14] HOU Z Y, TANG X Y, LUO X F, *et al*. A green synthetic route to the highly efficient K_2SiF_6:Mn^{4+} narrow-band red phosphor for warm white light-emitting diodes [J]. *J. Mater. Chem.* C, 2018, 6(11): 2741-2746.

[15] BLASSE G, BRIL A. A new phosphor for flying-spot cathode-ray tubes for color television: yellow-emitting $Y_3Al_5O_{12}$-Ce^{3+} [J]. *Appl. Phys. Lett.*, 1967, 11(2): 53-55.

[16] CHEN L, LIN C C, YEH C W, *et al*. Light converting inorganic phosphors for white light-emitting diodes [J]. *Materials*, 2020, 3(3): 2172-2195.

[17] PAN Z F, LI W Q, XU Y, *et al*. Structure and redshift of Ce^{3+} emission in anisotropically expanded garnet phosphor $MgY_2Al_4SiO_{12}$:Ce^{3+} [J]. *RSC Adv.*, 2016, 6(25): 20458-20466.

[18] JI H P, WANG L, MOLOKEEV M S, *et al*. Structure evolution and photoluminescence of $Lu_3(Al,Mg)_2(Al,Si)_3O_{12}$:$Ce^{3+}$ phosphors: new yellow-color converters for blue LED-driven solid state lighting [J]. *J. Mater. Chem.* C, 2016, 4(28): 6855-6863.

[19] SETLUR A A, HEWARD W J, GAO Y, *et al*. Crystal chemistry and luminescence of Ce^{3+}-doped $Lu_2CaMg_2(Si,Ge)_3O_{12}$ and its use in LED based lighting [J]. *Chem. Mater.*, 2006, 18(14): 3314-3322.

[20] XIA Z G, POEPPELMEIER K R. Chemistry-inspired adaptable framework structures [J]. *Acc. Chem. Res.*, 2017, 50(5): 1222-1230.

[21] EGGER D A, RAPPE A M, KRONIK L. Hybrid organic-inorganic perovskites on the move [J]. *Acc. Chem. Res.*, 2016, 49(3): 573-581.

[22] 苏彬彬, 夏志国. 新兴零维金属卤化物的光致发光与应用研究进展[J]. 发光学报, 2021, 42(6): 733-754.
SU B, XIA Z G. Research progresses of photoluminescence and application for emerging zero-dimensional metal halides luminescence materials[J]. *Chin. J. Lumin.*, 2021, 42(6): 733-754. (in Chinese)

[23] SUN Y M, FERNÁNDEZ-CARRIÓN A J, LIU Y H, *et al.* Bismuth-based halide double perovskite $Cs_2LiBiCl_6$: crystal structure, luminescence, and stability[J]. *Chem. Mater.*, 2021, 33(15): 5905-5916.

[24] MAJHER J D, GRAY M B, STROM T A, *et al.* $Cs_2NaBiCl_6:Mn^{2+}$—a new orange-red halide double perovskite phosphor[J]. *Chem. Mater.*, 2019, 31(5): 1738-1744.

[25] HOLZAPFEL N P, MAJHER J D, STROM T A, *et al.* $Cs_4Cd_{1-x}Mn_xBi_2Cl_{12}$—a vacancy-ordered halide perovskite phosphor with high-efficiency orange-red emission[J]. *Chem. Mater.*, 2020, 32(8): 3510-3516.

[26] ZHANG X Y, SUN J F. Intense blue emission of perovskite-type fluoride phosphor $Cs_4Mg_3CaF_{12}:Eu^{2+}$ as a promising pc-WLEDs material[J]. *J. Alloys Compd.*, 2020, 835: 155225.

[27] CHAI K, CHENG S C, LI H Y, *et al.* Modulation of perovskite-related frameworks induced by alkaline earth metals in phosphate fluorides A_2MPO_4F(A=K, Rb; M=Ba, Ca)[J]. *New J. Chem.*, 2019, 43(20): 7839-7845.

[28] DAICHO H, SHINOMIYA Y, ENOMOTO K, *et al.* A novel red-emitting $K_2Ca(PO_4)F:Eu^{2+}$ phosphor with a large Stokes shift[J]. *Chem. Commun.*, 2018, 54(8): 884-887.

[29] LI Y, QIU Z X, ZHANG J L, *et al.* Highly efficient and thermally stable single-activator white-emitting phosphor $K_2Ca(PO_4)F:Eu^{2+}$ for white light-emitting diodes[J]. *J. Mater. Chem.* C, 2019, 7(29): 8982-8991.

[30] WU D W, SHI C, ZHOU J C, *et al.* Full-visible-spectrum lighting enabled by site-selective occupation in the high efficient and thermal stable $(Rb,K)_2CaPO_4F:Eu^{2+}$ solid-solution phosphors[J]. *Chem. Eng. J.*, 2022, 430: 133062-1-10.

[31] ZHANG R, SUN J F. An efficient perovskite-type $Rb_2CaPO_4F:Eu^{2+}$ phosphor with high brightness towards closing the cyan gap[J]. *J. Alloys Compd.*, 2021, 872: 159698-1-16.

[32] ZHANG M S, CHANG L X, WANG L, *et al.* Synthesis, structure and electronic structure calculation of a new perovskite-type phosphate fluoride K_2BaPO_4F[J]. *Inorg. Chem. Commun.*, 2018, 93: 110-114.

[33] ZHAO M, ZHOU Y Y, MOLOKEEV M S, *et al.* Discovery of new narrow-band phosphors with the UCr_4C_4-related type structure by alkali cation effect[J]. *Adv. Opt. Mater.*, 2019, 7(6): 1801631-1-9.

[34] LENG Z H, ZHANG D, BAI H, *et al.* A zero-thermal-quenching perovskite-like phosphor with an ultra-narrow-band blue-emission for wide color gamut backlight display applications[J]. *J. Mater. Chem.* C, 2021, 9(39): 13722-13732.

[35] WU X L, SHI R, ZHANG J L, *et al.* Highly efficient and zero-thermal-quenching blue-emitting Eu^{2+}-activated K-beta-alumina phosphors[J]. *Chem. Eng. J.*, 2022, 429: 132225-1-10.

[36] KIM Y H, ARUNKUMAR P, KIM B Y, *et al.* A zero-thermal-quenching phosphor[J]. *Nat. Mater.*, 2017, 16(5): 543-550.

[37] LIU Y F, ZHANG C H, CHENG Z X, *et al.* Origin and luminescence of anomalous red-emitting center in rhombohedral $Ba_9Lu_2Si_6O_{24}:Eu^{2+}$ blue phosphor[J]. *Inorg. Chem.*, 2016, 55(17): 8628-8635.

[38] FENG N N, TIAN Y, WANG L, *et al.* Band structure, energy transfer and temperature-dependent luminescence of novel blue emitting $KBaYSi_2O_7:Eu^{2+}$ phosphor[J]. *J. Alloys Compd.*, 2016, 654: 133-139.

[39] WANG X, WANG J, LI X Y, *et al.* Novel bismuth activated blue-emitting phosphor $Ba_2Y_5B_5O_{17}:Bi^{3+}$ with strong NUV excitation for WLEDs[J]. *J. Mater. Chem.* C, 2019, 7(36): 11227-11233.

[40] TOBY B H. *EXPGUI*, a graphical user interface for *GSAS*[J]. *J. Appl. Crystallogr.*, 2001, 34(2): 210-213.

[41] NIELSEN O H, MARTIN R M. First-principles calculation of stress[J]. *Phys. Rev. Lett.*, 1983, 50(9): 697-700.

[42] PERDEW J P, BURKE K, ERNZERHOF M. Generalized gradient approximation made simple[J]. *Phys. Rev. Lett.*, 1996, 77(18): 3865-3868.

[43] 张少伯, 杨秋红, 胡娟. $ZrSiO_4:Mn^{4+}$荧光粉的制备及光谱性能[J]. 人工晶体学报, 2021, 50(8): 1438-1443.
ZHANG S B, YANG Q H, HU J. Synthesis and spectroscopic properties of $ZrSiO_4:Mn^{4+}$ phosphor[J]. *J. Synth. Cryst.*, 2021, 50(8): 1438-1443. (in Chinese)

[44] SHANNON R D. Revised effective ionic radii and systematic studies of interatomic distances in halides and chalcogenides[J]. *Acta Cryst.* A, 1976, 32(5): 751-767.

[45] SUN J F, ZHANG W L, SHI Y M, *et al.* Green-emitting $Ca_6Sr_4(Si_2O_7)_3Cl_2:Eu^{2+}$ phosphors for white light-emitting diodes[J]. *J. Electrochem. Soc.*, 2011, 159(1): J5-J12.

[46] KUBELKA P. New contributions to the optics of intensely light-scattering materials. Part I [J]. *J. Opt. Soc. Am.*, 1948, 38(5): 448-457.

[47] ZHANG W L, SUN J F, WANG X Q, *et al*. Crystal growth and optical properties of a noncentrosymmetric molybdenum tellurite, $Na_2Te_3Mo_3O_{16}$ [J]. *CrystEngComm*, 2012, 14(10): 3490-3494.

[48] XIAO Y, HAO Z D, ZHANG L L, *et al*. An efficient blue phosphor $Ba_2Lu_5B_5O_{17}$:Ce^{3+} stabilized by La_2O_3: photoluminescence properties and potential use in white LEDs [J]. *Dyes Pigm.*, 2018, 154: 121-127.

[49] ZHANG X G, SONG J H, ZHOU C Y, *et al*. High efficiency and broadband blue-emitting $NaCaBO_3$:Ce^{3+} phosphor for NUV light-emitting diodes [J]. *J. Lumin.*, 2014, 149: 69-74.

[50] SHANG M M, LI G G, GENG D L, *et al*. Blue emitting $Ca_8La_2(PO_4)_6O_2$:Ce^{3+}/Eu^{2+} phosphors with high color purity and brightness for white LED: soft-chemical synthesis, luminescence, and energy transfer properties [J]. *J. Phys. Chem. C*, 2012, 116(18): 10222-10231.

[51] TALWAR G J, JOSHI C P, MOHARIL S V, *et al*. Combustion synthesis of $Sr_3MgSi_2O_8$:Eu^{2+} and $Sr_2MgSi_2O_7$:Eu^{2+} phosphors [J]. *J. Lumin.*, 2009, 129(11): 1239-1241.

[52] LEE S H, KOO H Y, KIM J H, *et al*. $BaMgAl_{10}O_{17}$:Eu^{2+} phosphor powders prepared from precursor powders with a hollow and thin wall structure containing NH_4F flux [J]. *Electron. Mater. Lett.*, 2010, 6(2): 81-86.

[53] DEXTER D L. A theory of sensitized luminescence in solids [J]. *J. Chem. Phys.*, 1953, 21(5): 836-850.

[54] ZHANG X J, HUANG L, PAN F J, *et al*. Highly thermally stable single-component white-emitting silicate glass for organic-resin-free white-light-emitting diodes [J]. *ACS Appl. Mater. Interfaces*, 2014, 6(4): 2709-2717.

[55] HUANG S, SHANG M M, YAN Y, *et al*. Ultra-broadband green-emitting phosphors without cyan gap based on double-heterovalent substitution strategy for full-spectrum WLED lighting [J]. *Laser Photonics Rev.*, 2022, 16(12): 2200473.

张荣(1999-),女,陕西西安人,博士研究生,2021年于河北工业大学获得硕士学位,主要从事稀土发光材料的研究。

E-mail: zhangrong@hebut.edu.cn

孙剑锋(1983-),男,辽宁辽阳人,博士,副教授,2014年于清华大学获得博士学位,主要从事稀土发光材料的研究。

E-mail: sunjianfeng10@hebut.edu.cn